Thermally Enhanced Electro-osmosis to Control Foam Stability

Oriane Bonhomme, Li Peng, Anne-Laure Biance

Thermally Enhanced Electro-osmosis to Control Foam Stability

Oriane Bonhomme,[*] Li Peng, and Anne-Laure Biance[†]
Institut Lumière Matière, UMR5306 du CNRS, Université Lyon 1, 43 Bd du 11 Novembre 1918, 69622 Villeurbanne, France

(Received 9 December 2019; revised manuscript received 30 January 2020; accepted 12 March 2020; published 21 April 2020)

Liquid foam is a dense dispersion of liquid bubbles in a surfactant solution. Because of its large surface area, it is an out-of-equilibrium material that evolves with space and time because of coarsening, coalescence, and liquid drainage. In many applications, it is required to control the lifetime of a foam by limiting the drainage or triggering the collapse at a specific location or a given time. We show here that applying an external electric field at the edge of the foam induces some liquid flows. Depending on the flow magnitude, it controls either gravity driven drainage, the foam stability, or the foam collapse at a specific location. Thus, applying an electric field to a liquid foam can control its stability. The experimental results are quantitatively described by a simple model taking into account first the electro-osmotic transport in such a deformable medium and second the Marangoni flows induced by heterogeneous heating due to Joule effect. More specifically, we show for the first time that electro-osmosis can be strongly enhanced due to thermal gradients generated by the applied electric field.

DOI: 10.1103/PhysRevX.10.021015

Subject Areas: Fluid Dynamics, Materials Science, Soft Matter

I. INTRODUCTION

Controlling ion and liquid transport in nanofluidic membranes is crucial to develop emerging technologies for energy harvesting, filtration, or desalination [1]. In all these systems, a coupling between the electric field used to generate ion transport and Joule heating emerges. Such a coupling is important in biophysical applications [2], where liquid boiling and nanobubble formation have even been reported [3]. To understand how this coupling takes place, it is crucial to consider the geometry of the nanofluidic membrane. For example, investigating only ion or solute transports, the geometry has been optimized to generate functional devices such as nanofluidic diodes or transistors [4–7]. Regarding thermal effects, if the membrane is asymmetrical, so is the Joule heating, then thermal gradients are induced. These nonlinear thermal gradients will result in flows [8] and open the way for new functionalities. We use here, for the first time, this phenomenon of electrically induced thermal heating in a model structure made of heterogeneous deformable membranes, a liquid foam, to control its stability.

Controlling liquid foam lifetime and homogeneity is a real challenge for many applications, such as aerated materials manufacturing. Indeed, they are extensively used for their lightness, their thermal [9] or acoustic insulating properties, their green efficiency in the building industry [10], and more specifically their large surface area [11]. Recently, these aerated materials have been used, for example, as electrodes for supercapacitors or batteries [12], or as so-called thermal resonators for energy harvesting [13]. Their fabrication often relies on a two-step process, which consists in shaping the liquid and then solidifying it. Over all possible techniques, the cheapest and most ecological way is to template water-based liquid foams and then smoothly solidify the structure. However, liquid foams are out-of-equilibrium materials which evolve and collapse [14] due to coarsening, gravity-driven drainage, and coalescence [15,16]. Even if a large effort has been engaged to understand these intricate mechanisms [16], only a few strategies have been put forward to fabricate a liquid foam homogeneous in space and time. The most promising one, investigated only in two dimensions, is the use of thermal gradients [17] to drive the liquid flow in the foam structure thanks to Marangoni stresses generated along the interface. However, setting such gradients remains complicated and limited to microfluidic systems [18,19]. Otherwise, one can also want to destabilize a liquid foam for different purposes: in flotation or in decontamination processes, it is interesting to, at the end of the process, destabilize the material. Stabilizing or destroying a foam on demand has now become a crucial issue.

[*]oriane.bonhomme@univ-lyon1.fr
[†]anne-laure.biance@univ-lyon1.fr

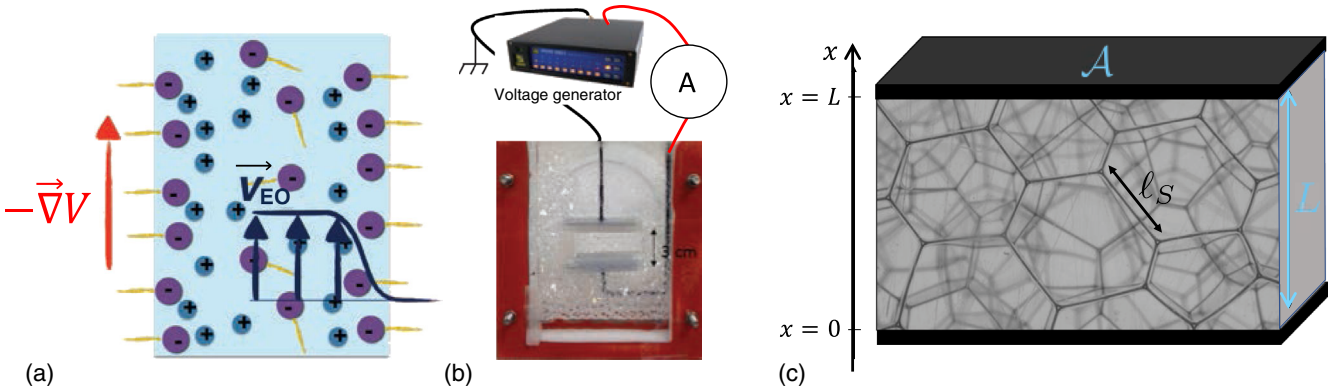

FIG. 1. (a) Scheme of electro-osmotic flow that takes place in a foam film. (b) Experimental setup allowing the study of electrokinetic transport in a macroscopic foam. (c) Side view picture of the foam between the electrodes; the focus is on the front plate.

Applying an external electric field to the foam will create a flow of liquid. This flow can affect locally the liquid fraction of the foam, and then its stability. In the case of foams stabilized with common ionic surfactants, the electric field induces an electro-osmotic flow in the liquid [20–22]. Generating an electro-osmotic flow at the vicinity of an interface covered with ionic surfactants has already been thoroughly investigated [20,22–27], even at the scale of a soap film [28]. The ionic surfactants adsorbed at the interface generate a cloud of counterions in the vicinity of the surface [29], which can be dragged by an electric field $\vec{E}$ applied tangentially to the interface [Fig. 1(a)]. The velocity of the liquid far from the interface is known to be proportional to this tangential electric field. It reads $\vec{v}_{EO} = -(\epsilon\zeta/\eta)\vec{E}$, with ϵ and η, respectively, the liquid permittivity and viscosity, and ζ the zeta potential of the interface, a signature of its electrostatic and hydrodynamic environment [30].

In this work, we show that an electric field can indeed generate a flow in a 3D macroscopic foam, and even reverse gravity-driven drainage. More interestingly, we show that the electric field can also trigger the destabilization of the foam above a critical electric field magnitude. Finally, we experimentally demonstrate that the electric field also heats up the foam heterogeneously, inducing thermal gradients and subsequent thermal and solutal Marangoni flows in the system. We highlight that both effects have to be included in the analysis to quantitatively describe our experimental results.

II. EXPERIMENTS

A. Material and methods

A liquid foam is generated by injecting air in a soapy solution through a needle in a tank [Fig. 1(b)] at a constant pressure of 50 mbar. Bubbles of a given size are generated, their mean radius being controlled by the needle diameter. The solution is made of sodium dodecyl sulfate (SDS) (from Sigma Aldrich, which reports a critical micellar concentration of 7–10 mmol/L, and used as received), dissolved in water at a concentration 0.01 mol/L. The surfactant solution was prepared everyday to avoid hydrolysis and creation of dodecanol. The surface tension of the solution is equal to $\gamma = 34$ mN/m. Its bulk conductivity has been measured with a commercial conductimeter (Hannah Instrument) and is equal to $\sigma_{SDS} \simeq 600$ μS/cm. The soapy solution was put in a plexiglas tank of dimension $10 \times 4.5 \times 13$ cm^3.

The bubble size is evaluated by measuring with ImageJ the length ℓ_S of the Plateau borders contacting the front surface. This length is then averaged over 100 measurements, and the bubble size is determined by the geometrical relationship linking the sizes of a Plateau border at the surface and in the bulk [31], $\ell \simeq \ell_S/1.2$, for a polydispersity around 20% in good agreement with our experiments. The bubble radius is determined assuming we have a Kelvin cell and is linked to the length of the Plateau border by $R \simeq 1.39\ell$ [32]. The bubble radius is varied between 0.8 and 5 mm, with a standard deviation of 20%. Averaged values of bubble size are reported in Table I.

The foam is squeezed between two horizontal electrodes of area $\mathcal{A}$ separated by a distance L. Electrodes are inox plates embedded in an agarose gel [Fig. 1(b)] to avoid the release of electrochemical wastes in the foam due to reactions at the electrodes. The electrode dimensions are 25×50 mm^2 and they are separated by a distance L between 20 and 40 mm ensuring to have at least five bubble layers in between the electrodes. The agarose gel is fabricated by mixing agar-agar (2%) in the SDS solution used above, by heating at 200 °C for 30 min, pouring the

TABLE I. Values of the different averaged quantities in our experiments, calculated or experimentally measured. Radius R is in mm, the initial conductance G_i in μS, the initial liquid fraction ϕ_i in %, times τ_c and τ_{max} are in seconds (s), the critical electric field E_c in V/mm, and Bo is the Bond number [Eq. (4)].

R (mm)	G_i (μS)	ϕ_i (%)	τ_{max} (s)	E_c (V/mm)	Bo	τ_c (s)
1.0±0.2	25.2±4.8	1.4 ± 0.3	44 ± 22	<2.5	2.6	40
2.6±0.6	8.4 ± 1.4	0.47±0.08	21 ± 7	≈6	3.8	28
4.3±0.9	3.2 ± 0.7	0.26±0.06	29 ± 9	≈11	4.2	42

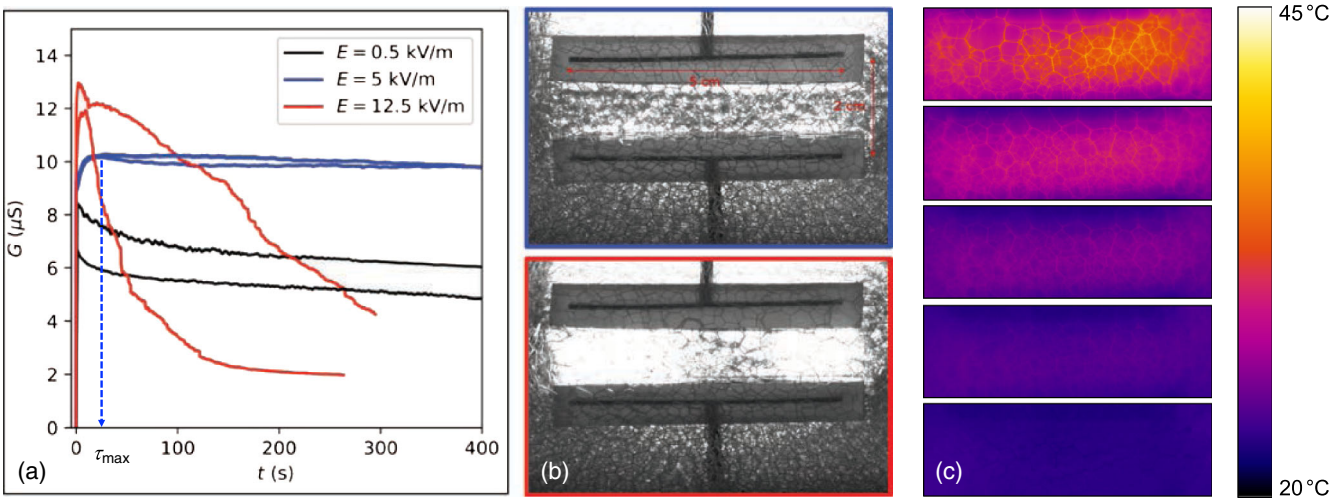

FIG. 2. (a) Conductance G of the foam as a function of time for different applied electric fields. In each case, two curves in the same conditions are superimposed. $R = 4.3$ mm, $\phi_i = 0.26\%$, $L = 20$ mm. The time $\tau_{\max}$ corresponds to the time at which the conductance reaches a maximum. (b) Snapshots of foam for $\Delta V = 100$ V (top) and $\Delta V = 500$ V (bottom), $R = 2.6$ mm, $\phi_i = 0.47\%$, $L = 20$ mm. (c) Infrared camera images of the foam for different applied voltages (from bottom to top: 200, 400, 600, 800, 1000 V). $R = 3.7$ mm, $\phi_i = 0.11\%$, $L = 29$ mm. Image height corresponds to 22.6 mm.

solution around the electrode in a designed tank, and cooling for 2 h. The gel is then cut into the specific shape. The conductivity of the agar gel embedding the electrodes has been thoroughly characterized and measured at $\sigma_{\text{gel}} = 730\ \mu\text{S/cm}$. It is large compared to the conductance of the foam of the order of 1–10 μS/cm, so fully negligible in our experiments.

These electrodes are plugged to a high-voltage generator (HVS448 High Voltage Sequencers, Labsmith) to apply a voltage difference $\Delta V = V(L) - V(0)$ between the electrodes. This creates an electric field $\vec{E} = -\Delta V/L\vec{e_x}$ which induces a flow from the bottom to the top: then the top electrode is fixed at a zero potential and the bottom one is fixed at voltage between 0 and 500 V. The ionic current I inside the foam is recorded with a homemade current-voltage convertor and amplifier. A camera (μeye, IDS) allows a side view of the sample within the electrodes.

The initial liquid fraction of the foam ϕ_i is defined as the ratio of the liquid volume over the entire volume of the foam and depends on the foam generation procedure. It is then evaluated by conductance measurements of the foam through $G_i = I/\Delta V = \sigma_F \mathcal{A}/L$, with $\sigma_F = \sigma_{\text{SDS}}\phi_i/3$ the foam conductivity (see the Appendix A). The liquid fraction is found to vary between 0.2% and 1.5% at initial stages (Table I).

Finally, the temperature of the foam has been measured using an infrared (IR) camera (X6580SC, FLIR Systems AB, 640x512px). For that purpose, one of the plexiglas vertical walls of the tank has been replaced by a Mylar sheet of thickness 50 μm, allowing IR transmission. IR output of the camera has been calibrated filling the tank with the surfactant solution at different temperatures (measured *in situ* with a commercial thermometer, TSPO1, Thorlabs). To overcome the heterogeneity of the temperature between the bubbles and the liquid, profiles have been calculated by horizontal line averaging. If the absolute value of the temperature must be taken cautiously due to the complexity of the medium, the global temperature variation can be discussed safely. Each data point of Fig. 3(b) corresponds to an average on 4–6 experiments.

B. Stability of the foam

Typical results of the variations of the conductance ($G = I/\Delta V$) versus time for different applied voltages are reported in Fig. 2(a). Three distinct situations are observed. At zero and low voltages [typically $\Delta V \approx -10$ V, black curve in Fig. 2(a)], the conductance is decreasing with time, to reach a plateau after a few hundreds of seconds. At intermediate voltages [for example, $\Delta V \approx -100$ V, blue curve in Fig. 2(a)], the conductance first increases, reaches a maximum after a few tens of seconds, and then decreases to reach a plateau after a few hundreds of seconds. The signal is stable for more than 40 min. At larger voltages [typically $\Delta V \approx -500$ V, red curve in Fig. 2(a)], the conductance reaches a maximum and then decreases abruptly (more than 20% after 200 s). Side view images show that in the latter case the light is transmitted through the sample, a signature of foam collapse.

Several quantities are measured and reported in Table I. First, in the regime where a maximum is observed, the time to reach this maximum $\tau_{\max}$ is almost independent of the field intensity, but varies with the bubble size and the initial liquid fraction. Second, the critical electrical field E_c at which collapse occurs increases also with the bubble size (see Table I).

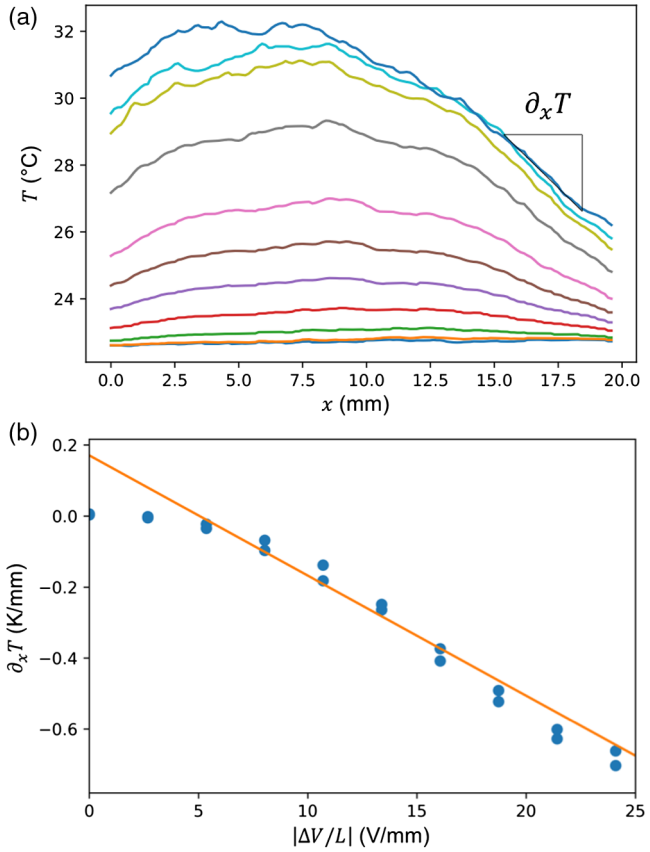

FIG. 3. (a) Stationary temperature profile (after 50 s) for different applied voltage ($L = 19$ mm, $R = 3.7$ mm, and $\phi_i = 0.11\%$). Voltage varies from 0 to 1000 V with a 100 V step from bottom to top. The black line shows the fit used to extract the temperature gradient for 1000 V. (b) Temperature gradient at the top of the foam deduced from a linear fit of temperature profile [see (a)]. The line is a linear fit, $\partial_x T = -kE + b$, with $k = 0.034$ K/V and $b = 0.18$ K/mm.

C. Temperature profile within the foam

Typical thermal maps of the foam sample obtained at different applied voltages are reported in Fig. 2(c). When an electric current runs through the foam, a heterogeneous temperature profile is established. Indeed, as the liquid fraction is heterogeneous, the foam conductance (and thus its electric resistance) is heterogeneous too, and the Joule effect magnitude will be different on the different parts of the foam. We thus recorded the temperature within the foam and observed that a thermal stationary state is reached after typically 50 s. To characterize more quantitatively this effect, we analyzed the infrared images of the foam sample and we measured the temperature in the foam sample, averaged horizontally, as a function of the altitude x. Typical steady-state temperature profiles are reported in Fig. 3(a) for different applied voltages. The temperature is clearly heterogeneous between the two electrodes. Neglecting the vicinity of the bottom electrode, a strong temperature gradient from the bottom to the top is observed. The absolute value of the temperature T within the foam indeed increases with the applied voltage difference but associated thermal gradient also does. At first order, we will only consider the linear variation of the temperature profile close to the top electrode. By fitting the right part of the temperature profile, we measured the magnitude of the negative thermal gradient close to the top electrode. We reported it as a function of the applied voltage in Fig 3(b). We fit these variations linearly: $\partial_x T = -kE + b$, with $k = 0.034$ K/V and $b = 0.18$ K/mm.

III. MODEL OF ELECTROKINETIC TRANSPORT IN A LIQUID FOAM

To interpret these experimental observations, we estimate the liquid fraction profile $\phi(x,t)$ within the foam. We model the foam by a continuous medium [33] of length L and area $\mathcal{A}$, the x direction is taken vertically, upward. We recall here that the voltage gradient is downward to ensure a flow that counteracts gravity. Notations are reported in Fig. 1(c). Electrokinetic transport in a porous medium, like a foam, is well described by a linear response through the symmetrical Onsager matrix [34,35]. If we note Q the mass flow rate, I the ionic current, $\partial_x P + \rho g$ the pressure gradient, $\partial_x T$ the temperature gradient and $\partial_x V$ the electric potential gradient in the system, it reads [33,36]:

$$\begin{aligned} Q &= -\mathcal{A}\left[L_H\left(\frac{\partial P}{\partial x} + \rho g\right) + \alpha\frac{\partial V}{\partial x} + \alpha_T\frac{\partial T}{T\partial x}\right], \\ I &= -\mathcal{A}\left[\alpha\left(\frac{\partial P}{\partial x} + \rho g\right) + \sigma_F\frac{\partial V}{\partial x} + S_T\frac{\partial T}{T\partial x}\right], \end{aligned} \tag{1}$$

with L_H the permeability, α the electro-osmotic mobility, σ_F the electric conductivity, α_T the thermo-osmotic mobility, and where S_T, the thermoelectric coefficient, characterizes the so-called Seebeck effect (conversion of heat into electricity); see Appendix A. To determine the liquid fraction profile within the system, we apply mass conservation within the foam sample: $\mathcal{A}\partial_t\phi = -\partial_x Q$. Keeping only dominant terms in this equation (see Appendix B), we derive the following approximated single differential equation for $\phi(x,t)$:

$$\frac{\partial\phi(x,t)}{\partial t} \simeq \frac{\partial}{\partial x}\left[\left(\frac{\partial P}{\partial x} + \rho g\right)L_H\right]. \tag{2}$$

A liquid foam is a peculiar case of porous media, called poroelastic media. Thus, the different coefficients are a function of the foam characteristics (bubble size, surfactant nature) but also depend on the local liquid fraction $\phi(x,t)$.

Concerning the hydrodynamic permeability of the foam L_H, two limiting cases can be considered: whether the dissipation takes place in the Plateau borders (small channels connecting three films in the foam structure [15]) or in the nodes, at the intersection of the Plateau

borders. With the surfactant solution used here (made of SDS), we expect a zero velocity condition at the interface [37,38] and then choose the first case. Then, the hydrodynamic permeability reads $L_H = (K_H/\eta)R^2\phi^2$, with $K_H = 0.0032$ and η the suspending liquid dynamic viscosity [39].

Moreover, a relationship links the local pressure gradient to the local liquid fraction. Indeed, the radius of curvature of the Plateau borders adapts to the local pressure, which then fixes their width and consequently the amount of liquid that they contain. More precisely, noting γ the liquid-gas surface tension, and β being a numerical factor close to 0.6 [40], the capillary pressure gradient within the foam depends on $\phi(x,t)$ and reads $\partial_x P = \frac{1}{2}\beta(\gamma/R)(1/\phi^{3/2})\partial_x\phi$.

Replacing explicitly the pressure gradient and the expression of L_H, and after rendering quantities dimensionless, Eq. (2) reduces to

$$\frac{\partial\bar{\phi}(X,\tau)}{\partial\tau} \simeq \frac{\partial}{\partial X}\left[\mathrm{Bo}\bar{\phi}(X,\tau)^2 + \frac{\partial\bar{\phi}(X,\tau)}{\partial X}\sqrt{\bar{\phi}(X,\tau)}\right], \tag{3}$$

where the dimensionless quantities are defined as $\tau = t/\tau_c$, with $\tau_c = 2\eta L^2/(\gamma\beta K_H R\sqrt{\phi_i})$, and $\bar{\phi} = \phi/\phi_i$, with ϕ_i the initial liquid fraction, and $X = x/L$. Bo is the so-called Bond number, which compares gravity and capillary pressure gradient, adapted to foams according to

$$\mathrm{Bo} = \frac{2\rho g L R\sqrt{\phi_i}}{\gamma\beta}. \tag{4}$$

One can notice that Eq. (3) is reminiscent of the equation that governs free drainage in a liquid foam due to gravity [39–41]. To set orders of magnitude, the averaged values of the Bond number Bo and of the characteristic time τ_c for our experimental configurations are reported in Table I.

This equation is completed with two boundary conditions. We first assume that the foam between the electrodes is isolated from the outside. Then, volume conservation reads:

$$\int_0^1 \bar{\phi}(X,\tau)dX = 1. \tag{5}$$

The other assumption is that the electrodes are impermeable (no flux). This is justified by comparing the permeability of the agarose gel ($\kappa \approx 600$ nm^2 [42]) and the permeability of the foam ($L_H\eta \approx 3\times10^8$ nm^2 with $R \approx 1$ mm and $\phi \approx 1\%$). It then reads $Q(0) = Q(L) = 0$, which can be reduced to

$$\left[L_H\left(\frac{\partial P}{\partial x} + \rho g\right) + \alpha\frac{\partial V}{\partial x} + \alpha_T\frac{1}{T}\frac{\partial T}{\partial x}\right]\Bigg|_{x=0,L} = 0. \tag{6}$$

The second term corresponds to the electro-osmotic flux of matter in the foam due to an applied tangential electric field. It depends on α which reads $\alpha = -(\phi\epsilon\zeta)/(3\eta)$ [33] (Appendix A). The third one corresponds to the flux of matter induced by a thermal gradient through the transport coefficient $\alpha_T = (T\phi\ell_T\partial_T\gamma)/(3\eta)$ with ℓ_T a characteristic thermal length scale and $\partial_T\gamma$ the variations of surface tension as a function of the temperature. At a first order, and in agreement with the experimental observations, we will consider that the thermal gradient is a linear function of the voltage difference [Fig. 3(b)]. Moreover, we consider that the temperature variations due to heating are small compared to the absolute temperature of the system $\partial_x TL/T \ll 1$, then that the absolute temperature T in the foam is constant.

This set of equations [Eqs. (3), (5), and (6)] can be solved in steady state. In this case, the liquid fraction is independent of time [$\partial_\tau\bar{\phi}(X,\tau) = 0$, then $\bar{\phi}(X,\tau) = \bar{\phi}(X)$]. The global flux is independent of X [from mass conservation equation, Eq. (B1)] and equal to zero because of the impermeabilty of the electrodes [Eq. (6)]. Equation (6) is thus valid at each X and can be integrated between 0 and L, to obtain

$$\mathrm{Ca} = \mathrm{Bo} + 2\left[\sqrt{\bar{\phi}(1)} - \sqrt{\bar{\phi}(0)}\right], \tag{7}$$

where Ca is an effective capillary number built as the sum of a so-called electro-osmotic capillary number Ca_E that compares electro-osmotic entrainment and capillary suction in the foam,

$$\mathrm{Ca}_E = \frac{\phi_i\epsilon\zeta\Delta V}{3\eta L}\frac{2\eta L}{K_H R\beta\gamma\phi_i^{3/2}}, \tag{8}$$

and a so-called thermo-osmotic capillary number Ca_T, which compares thermal entrainment and capillary suction in the foam,

$$\mathrm{Ca}_T = \frac{\phi_i\ell_T k\partial_T\gamma\Delta V}{3\eta L}\frac{2\eta L}{K_H R\beta\gamma\phi_i^{3/2}}. \tag{9}$$

As defined here, those capillary numbers are positive because the zeta potential, the thermal dependence of the surface tension, and the voltage difference are negative quantities in our experimental conditions. We discuss the magnitude of each mechanism involved in this effective capillary number in the following.

IV. DISCUSSION

A. Reversing drainage and collapse of the foam at the critical electrical field

Steady-state liquid fraction profiles, obtained by numerical integration of Eqs. (3), (5), and (7), for different effective Ca numbers and at a given Bo of 5.3 (a value that is typical in our system) are reported in Fig. 4(a). At low Ca, the

liquid fraction decreases with the altitude (in agreement with gravity-driven drainage), whereas above a given capillary number, the contrary is observed. In that case, the drainage is inverted by the flows induced by the voltage difference. An inversion of the profile is observed, whatever the Bond number value, but occurs at different capillary numbers. From Eq. (7), the threshold to get an inverted profile is given by Ca = Bo.

The main feature we observe experimentally is the collapse of the foam at large applied voltage. To rationalize this observation, we first extract from Fig. 4(a) the dimensionless liquid fraction at the bottom of the foam column $\bar{\phi}(0)$, and report it in Fig. 4(b) as a function of the capillary number Ca. We observe that above a critical value of Ca, which depends on the Bond number Bo, the liquid fraction at the bottom of the foam decreases dramatically. Considering that a real foam is unstable when $\phi \leq 0.1\%$ [14], a theoretical critical capillary number $\mathrm{Ca}_{\mathrm{crit}}$ expected for the collapse can then be determined as a function of the Bond number Bo.

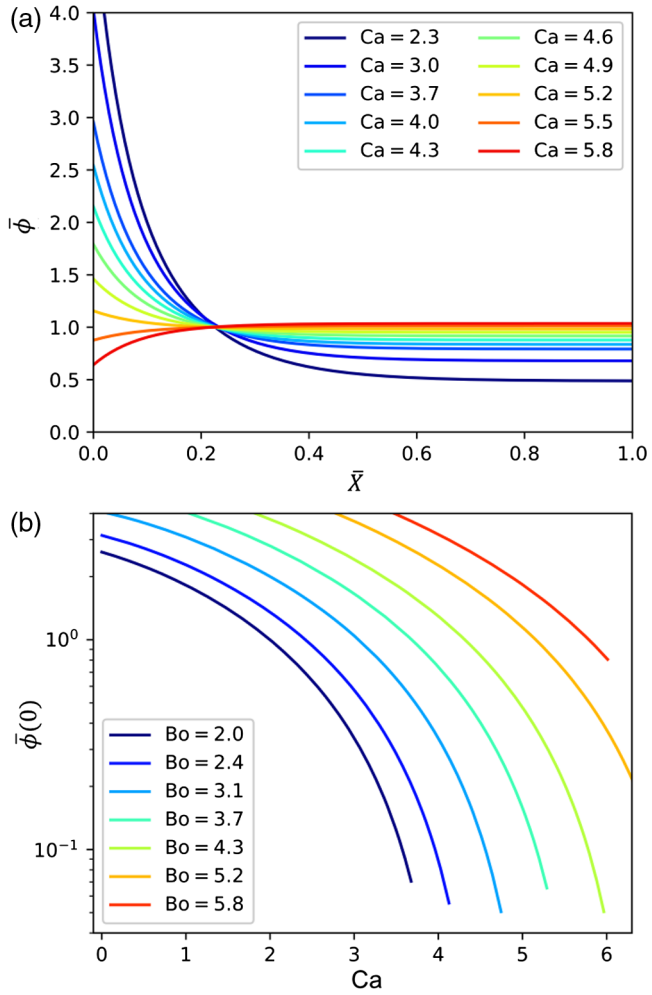

FIG. 4. (a) Evolution of the dimensionless liquid fraction $\bar{\phi}$ as a function of the dimensionless altitude X obtained numerically for a Bond number equal to 5.3 and different effective capillary numbers Ca. (b) Theoretically predicted dimensionless liquid fraction at the bottom of the sample $\bar{\phi}(0)$ as a function of the effective capillary number Ca for different Bond number Bo.

B. Combined thermal and electrical gradients induce drainage reversal

To compare these results with experiments, we need to link the theoretical critical capillary number to the value of a voltage difference through Eqs. (8) and (9). To that purpose, we consider a typical zeta potential of the SDS laden air-water interface of $\zeta = -100$ mV [20] and thermal dependence of surface tension $\partial_T \gamma = -2 \times 10^{-4}\ \mathrm{NK^{-1}\,m^{-1}}$ [43], which seems reasonable for the SDS solution used here. Moreover, we assume that the characteristic length on which the dissipation due to the interfacial stress occurs is of the order of the Plateau border length ($\ell_T \approx 100\ \mu$m).

Once these values are fixed, we determine the effective capillary and Bond numbers associated to each experimental conditions. We then plot on a (Bo;Ca) diagram (Fig. 5) the outcome of the experiments and the theoretical parameters (Bo;Ca) for which $\phi(0)$ was equal to 0.1%, and we find a quantitative agreement, given the accuracy of our model and our experiments.

Note that some uncertainties rely on the specific liquid fraction at which we assume that the destabilization of the foam would occur, a point still debated in literature [44]. But it hardly affects the location of the theoretical curve and of the critical capillary number at a given Bond number.

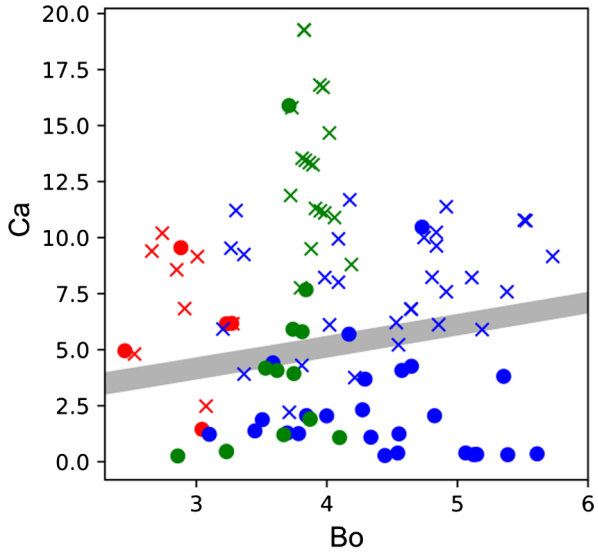

FIG. 5. Ca versus Bo experimental phase diagram. Symbols are associated to the mean bubble radius: red, $R = 1.0$ mm; blue, $R = 2.6$ mm; green, $R = 4.3$ mm. Plain circles represent stable foams and crosses represent foams where avalanches are reported. The continuous gray area is obtained numerically and corresponds to (Bo;Ca) values for which $\phi(0) = 0.1\%$ given the initial liquid fraction dispersion.

FIG. 6. Side view images (diffused reflected light) of the foam under 0 (left), 200 (middle) and 400 V (right) with a color camera ($L = 24$ mm, $R = 3$ mm, image height is 20 mm.)

Indeed, the variations of $\bar{\phi}(0)$ as a function of Ca are very sharp, as shown in the semilogarithmic scale plot of Fig. 4(b). This sharpness also explains why the critical capillary number for destabilization is close to the one for inversion [Ca = Bo, Eq. (7)].

To go further, one can note that the thermo-osmotic capillary number Ca_T is one order of magnitude larger than the electro-osmotic one Ca_E [typically, $\mathrm{Ca}_T/\mathrm{Ca}_E = (\ell_T k \partial_T \gamma)/(\epsilon\zeta) \approx 10$]. Then flow induced by thermal gradient dominates here. Neglecting thermal effect, and thus associating the effective capillary number to the electro-osmotic capillary number only, can explain the quite nonphysical zeta potential obtained in the literature in similar experiments [21].

C. Toward extended modeling

The simple model proposed here catches nearly quantitatively the experimental observations. Some justifications of the made assumptions and some possible refinements are discussed in the following.

1. Small solutal Marangoni stress at the interface

In the Plateau borders, three types of flow superimposed: a gravity-driven flow, an electro-osmotic flow, and a thermal Marangoni driven flow. Each of these flows induces stress at the interface, which could be compensated by a heterogeneous surfactant repartition along the interface and induce a subsequent solutal Marangoni stress. For the electro-osmotic flow, it has been shown theoretically, numerically, and experimentally [23,45] that no solutal Marangoni stress established and that the surfactants remain homogeneously distributed along the interface. Concerning the thermal Marangoni-induced flow, a solutal Marangoni stress can indeed establish [43], but not with SDS [17]. Finally, considering the gravity-driven flow, we use the permeability of a foam with so-called rigid interface, this rigidity being indeed induced by a solutal Marangoni stress. To give orders of magnitude, the pressure gradient is $\sim\rho g$, and then the viscous stress due to the flow along the interface is of the order of $\rho g r$, r being a typical width of the Plateau borders or the order of 10 μm. This induces a stress of 0.1 $\mathrm{N/m^2}$ along the interface, and then a surface tension difference of $\Delta\gamma \sim 0.1$ mN/m on one Plateau border. The difference of surface concentration associated to this surface tension variation is below 1% [46]. The zeta potential and the thermo-osmotic response due to temperature variations will then only be hardly modified, so their modifications are negligible.

2. Contribution of the films is small

During the experiments, the averaged color of the foam changes, as illustrated in Fig. 6, due to the thickening of the foam films. The contribution of the films is then increased. Previous experiments done at the scale of one film [28] show that this thickening indeed depends on the electric field magnitude as $\delta \sim r(\epsilon\zeta\Delta V/\gamma L)^{2/3}$, resulting in film thicknesses of the order of 100 nm. Taking into account the permeability of the films also, we estimate this extra contribution in our transport properties and show it was between 5% and 30% (see Appendix C).

3. Complex temperature profile

The temperature profile within the foam is more complex than simply linear, as shown in Fig. 3. Indeed, the foam has a complex shape and agarose electrodes might act as heat sources or thermostats (the heat capacity of the gel, close to the heat capacity of water due to its composition, is orders of magnitude larger than the one of the foam, made essentially of air). A full prediction of the complete temperature profile is then out of the scope of this paper. This profile is stationary, after a transient heating lasting around 40 s, depending on the conditions.

V. CONCLUSION

We experimentally show that some flows can be generated in a macroscopic liquid foam by applying an electric field. If the flow direction is well chosen, namely in the upward direction, it can increase the foam stability and counteract gravity-driven drainage. Moreover, above a critical electric field, the flow is sufficient to reverse the drainage. Then, if the liquid fraction at the bottom of the foam column becomes small enough, collapse will occur. We thus demonstrate that an electric field is a practical noninvasive technique to tune the properties of a foam and its homogeneity, and to control the foam collapse in a few tens of seconds. Similarly, we observe that combining the flows generated by the external electric field and by the gravity can be even more efficient to induce foam destruction.

The description of this process is fully apprehended by considering an electrically induced flow in such a

poroelastic medium. The electrically induced flow is due to electro-osmosis, but boosted by Joule effect. Indeed, in this complex material, the heating is heterogeneous and results in temperature gradients within the foam sample. These gradients generate additional Marangoni flows along the interface, whose magnitude is 10 times larger than classical electro-osmosis.

We then show for the first time that Joule heating contribution is crucial to understand electro-osmosis in such a heterogeneous medium, inducing thermal gradients and associated flows. The contribution of this electrically induced thermal heating in other asymmetric or deformable nanofluidic membranes on zeta-potential measurements is a new concept that remains to be explored.

ACKNOWLEDGMENTS

We would like to thank the ANR through the projects Blue Energy (ANR-14-CE05-0017) and NECtAR (ANR-16-CE06-0004-01) for funding. The authors acknowledge I. Cantat for fruitful discussion.

APPENDIX A: TRANSPORT COEFFICIENTS IN LIQUID FOAMS

We define here the different transport coefficients in a dry liquid foam. In all these definitions, the transport occurs mainly in the assembly of Plateau borders, meaning that the contribution of the films is neglected. This point is discussed in Appendix C.

Hydrodynamic permeability L_H.—The permeability L_H of the foam links the flow rate per unit area in this porous material to the pressure gradient that generates it. As commonly done for SDS solutions, we consider here that the interfaces are rigid; i.e., the velocity is assumed to be zero at the liquid-gas interface. Then, the permeability reads [40]:

$$L_H = \frac{K_H}{\eta} R^2 \phi^2, \tag{A1}$$

where $K_H = 0.0032$, η is the bulk viscosity, R is the bubble radius, and ϕ is the local liquid fraction.

Conductivity σ_F.—The conductivity σ_F of the foam is defined as the ratio between the electrical current per unit of area and the gradient of voltage applied to the foam. In the case of foams that are dry enough ($\phi \leq 5\%$), it follows the Lemlich formula [47]:

$$\sigma_F = \frac{\phi}{3}\sigma, \tag{A2}$$

where σ is the bulk conductivity of the solution.

Electro-osmotic mobility α.—The electro-osmotic mobility coefficient α links the flow rate per unit area due to the electro-osmotic flow and the applied electric field. The electro-osmotic flow is pluglike in channels larger than the Debye length [1] (here $\lambda_D \simeq 3$ nm) and its velocity reads $\vec{v}_{\mathrm{EO}} = -(\epsilon\zeta/\eta)\vec{E}$. We then make a direct analogy between the conductance and the electro-osmotic mobility in our system, stating that we have plug flows in a random assembly of Plateau borders:

$$\alpha = -\frac{\phi}{3}\frac{\epsilon\zeta}{\eta}, \tag{A3}$$

with ϵ the dielectric permittivity of the liquid and ζ the so-called zeta potential of the interface. For the SDS solution used here, the zeta potential is of the order of -100 mV; hence, $\alpha > 0$.

Thermo-osmotic mobility α_T.—The thermo-osmotic mobility coefficient α_T is defined as the ratio between the flow rate per unit area induced by the thermal gradient and the temperature gradient.

We assume at first order that the flow is induced by a thermal Marangoni stress. The velocity induced by the thermal gradient scales as $v_T \sim (\partial_x\gamma)\ell_T/\eta \sim (\partial_T\gamma)(\partial_x T)\ell_T/\eta$. $\partial_x\gamma$ ($\partial_T\gamma$) is the spatial (thermal) gradient in surface tension, $\partial_x T$ is the spatial temperature gradient, and ℓ_T is the characteristic length on which the dissipation due to the interfacial stress occurs. Considering that this thermally induced flow is pluglike in the Plateau borders, we assume that velocity variations will occur on the Plateau borders' length and thus assimilate ℓ_T to $\ell \sim 100$ μm.

Geometrically, we state that we have plug flows in a random assembly of Plateau borders. Thus by analogy to conductance, we obtain

$$\alpha_T = \frac{\phi}{3}\frac{\ell_T T \partial_T\gamma}{\eta}. \tag{A4}$$

For the SDS solution used here, $\alpha_T < 0$ as $\partial_T\gamma = -2 \times 10^{-4}$ Nm^{-1} K^{-1}.

Thermoelectric coefficient S_T.—This coefficient is much more difficult to establish for soapy interfaces. For classical interface, the usual interpretation [48] due to electrostatic force has been recently challenged by MD simulations [49]. If we note this transport coefficient M_{TE} in the vicinity of the interface, due to the foam geometry, it reads as for the other terms:

$$S_T = \frac{\phi}{3} M_{\mathrm{TE}}. \tag{A5}$$

Its extreme value is around 3 mC m^{-1} s^{-1}.

APPENDIX B: CALCULATION DERIVATION

The spatiotemporal liquid fraction profile can be calculated from the mass conservation equation:

$$\mathcal{A}\frac{\partial\phi(x,t)}{\partial t} = -\frac{\partial Q(x,t)}{\partial x}, \tag{B1}$$

where $Q(x,t)$ is the liquid flux in the foam.

In steady state, using first line of Eq. (1), it reads:

$$0 = \frac{\partial}{\partial x}\left[L_H\left(\frac{\partial P}{\partial x}+\rho g\right)+\left(\alpha-\frac{k\alpha_T}{T}\right)\frac{\partial V}{\partial x}\right]. \tag{B2}$$

We then use second line of Eq. (1) to link the potential gradient along the spatial direction to the pressure gradient:

$$\frac{\partial V}{\partial x} = \frac{1}{\sigma_F - kS_T/T}\left[\alpha\left(\frac{\partial P}{\partial x}+\rho g\right)+\frac{I(t)}{\mathcal{A}}\right]. \tag{B3}$$

The electrical current I is conserved through the sample, so it does not depend on the spatial coordinate in the steady-state regime. Then, Eq. (B2) reads:

$$0 = \frac{\partial}{\partial x}\left[\left(\frac{\partial P}{\partial x}+\rho g\right)\left(L_H-\frac{\alpha(\alpha-k\alpha_T/T)}{\sigma_F - kS_T/T}\right)\right]. \tag{B4}$$

We can safely neglect the second right-hand term by noting that $\{[\alpha(\alpha-k\alpha_T/T)]/[(\sigma_F-kS_T/T)L_H]\}$ is in the range 2×10^{-4} to 10^{-5} in our experimental conditions. The liquid fraction profile then satisfies:

$$\frac{\partial}{\partial x}\left[\left(\frac{\partial P}{\partial x}+\rho g\right)L_H\right] = 0, \tag{B5}$$

which is the steady-state version of Eq. (2).

APPENDIX C: FILM CONTRIBUTION

In the model, only the Plateau borders contribute to the liquid fraction evolution in the foam. The quantity of liquid flowing through the films is neglected, even though deviations due to films have already been suggested for gravity-driven drainage [50]. To take them into account, we first need to characterize the thickness of the films, and then to estimate how they contribute to transport.

In foams at equilibrium (with no flow) the film thickness is set to the equilibrium thickness [29], around 20 nm. However, one observes that when the voltage is on, the color of the foam is changing (Fig. 6), a signature of larger film thicknesses.

At the scale of one bubble [28], soap films thicken when an electro-osmotic flow occurs. The film thickness depends with a $2/3$ power-law dependency on the flow velocity and is proportional to the curvature radius of the meniscus (that act as reservoirs) at the ends of the film (r). With a similar analysis for combined electro-osmotic and thermal-driven flow, the film thickness obeys

$$\delta = 2.68r\left(\frac{(\epsilon\zeta+\ell_T k\partial_T\gamma)}{\gamma}\frac{\Delta V}{L}\right)^{2/3}, \tag{C1}$$

with ζ the zeta potential of the interface, γ the surface tension, ℓ_T a characteristic length of the thermal flow, k the proportionality coefficient between the temperature gradient and the voltage difference applied, and $\partial_T\gamma$ the surface tension gradient with respect to the temperature.

Then, the total liquid fraction has two contributions, one contribution from the Plateau borders ϕ_{Pb} and one from the films ϕ_{film}:

$$\phi = \phi_{\text{Pb}} + \phi_{\text{film}}, \tag{C2}$$

with, geometrically [15],

$$\phi_{\text{Pb}} \simeq 0.17\left(\frac{r}{\ell}\right)^2,$$
$$\phi_{\text{film}} \simeq 1.18\frac{\delta}{\ell}, \tag{C3}$$

which can now be defined for each experiment.

We estimate what will be the contribution of the films on the different parameters involved in our modeling.

1. On the permeability and on the capillary pressure

The contribution of the films on the hydrodynamic permeability L_H is negligible in our limit of rigid interfaces. Indeed, the dissipation in one film will scale as $\delta\ell^2\eta v/\delta^2$, 5000 times greater than in one Plateau border $r^2\ell\eta v/r^2$. So the flow in the films will be far smaller than in the Plateau borders. For determining L_H, the relevant liquid fraction is the one of the Plateau border ϕ_{Pb}.

Concerning the capillary pressure, it is governed directly by the shape of the Plateau borders, so in this case also, when estimating $\partial P/\partial x$, one has to take into account only ϕ_{Pb}.

2. On the conductance and on the electro-osmotic mobility

The contribution of liquid in the films on these two transport coefficients is proportional to ϕ_{film}, so when considering G and α, one has to consider the total liquid fraction ϕ.

3. On the transport equations

The main transport equation [Eq. (2)] remains written on ϕ_{Pb}. The first boundary condition, which imposes the volume conservation [Eq. (5)], remains valid. The second boundary condition, which corresponds to the impermeability of the elecrodes [Eq. (7)], is modified and now reads:

$$\text{Ca} = \text{Bo}\int_0^1 \frac{\bar{\phi}_{\text{Pb}}^2}{\bar{\phi}}dX + \int_0^1 \frac{\bar{\phi}_{\text{Pb}}^{1/2}}{\bar{\phi}(\partial\bar{\phi}_{\text{Pb}}/\partial X)}dX. \tag{C4}$$

4. On the critical capillary number

As in Sec. IV A, we obtain the liquid fraction profile through numerical integration and determine the critical capillary number at which the bottom liquid fraction becomes too low to keep a stable foam, taking into account film contribution. For example, for a bubble radius $R = 2.6$ mm, and a Bond number equal to 4, the critical capillary number obtained for foam collapse is 4.58 without film contribution and 4.1 taking into account the film thickening, a difference of 11%, below our experimental resolution.

[1] L. Bocquet and E. Charlaix, *Nanofluidics, from Bulk to Interfaces*, Chem. Soc. Rev. **39**, 1073 (2010).

[2] G. Nagashima, E. V. Levine, D. P. Hoogerheide, M. M. Burns, and J. A. Golovchenko, *Superheating and Homogeneous Single Bubble Nucleation in a Solid-State Nanopore*, Phys. Rev. Lett. **113**, 024506 (2014).

[3] R. M. M. Smeets, U. F. Keyser, M. Y. Wu, N. H. Dekker, and C. Dekker, *Nanobubbles in Solid-State Nanopores*, Phys. Rev. Lett. **97**, 088101 (2006).

[4] R. B. Schasfoort, S. Schlautmann, J. Hendrikse, and A. Van Den Berg, *Field-Effect Flow Control for Microfabricated Fluidic Networks*, Science **286**, 942 (1999).

[5] L.-J. Cheng and L. J. Guo, *Nanofluidic Diodes*, Chem. Soc. Rev. **39**, 923 (2010).

[6] Z. S. Siwy and S. Howorka, *Engineered Voltage-Responsive Nanopores*, Chem. Soc. Rev. **39**, 1115 (2010).

[7] L. Jubin, A. Poggioli, A. Siria, and L. Bocquet, *Dramatic Pressure-Sensitive Ion Conduction in Conical Nanopores*, Proc. Natl. Acad. Sci. U.S.A. **115**, 4063 (2018).

[8] B. Derjaguin and G. Sidorenkov, *On Thermo-osmosis of Liquid in Porous Glass*, C.R. Acad. Sci. URSS **32**, 622 (1941).

[9] B. Wicklein, A. Kocjan, G. Salazar-Alvarez, F. Carosio, G. Camino, M. Antonietti, and L. Bergström, *Thermally Insulating and Fire-Retardant Lightweight Anisotropic Foams Based on Nanocellulose and Graphene Oxide*, Nat. Nanotechnol. **10**, 277 (2015).

[10] P. Petit, I. Javierre, P.-H. Jézéquel, and A.-L. Biance, *Generation and Stability of Bubbles in a Cement Based Slurry*, Cement Concrete Res. **60**, 37 (2014).

[11] J. Deng, H. Li, S. Wang, D. Ding, M. Chen, C. Liu, Z. Tian, K. Novoselov, C. Ma, D. Deng, and X. Bao, *Multiscale Structural and Electronic Control of Molybdenum Disulfide Foam for Highly Efficient Hydrogen Production*, Nat. Commun. **8**, 14430 (2017).

[12] M.-C. Lin, M. Gong, B. Lu, Y. Wu, D.-Y. Wang, M. Guan, M. Angell, C. Chen, J. Yang, B.-J. Hwang, and H. Dai, *An Ultrafast Rechargeable Aluminium-Ion Battery*, Nature (London) **520**, 324 (2015).

[13] A. L. Cottrill, A. T. Liu, Y. Kunai, V. B. Koman, A. Kaplan, S. G. Mahajan, P. Liu, A. R. Toland, and M. S. Strano, *Ultra-High Thermal Effusivity Materials for Resonant Ambient Thermal Energy Harvesting*, Nat. Commun. **9**, 664 (2018).

[14] A.-L. Biance, A. Delbos, and O. Pitois, *How Topological Rearrangements and Liquid Fraction Control Liquid Foam Stability*, Phys. Rev. Lett. **106**, 068301 (2011).

[15] I. Cantat, S. Cohen-Addad, F. Elias, F. Graner, R. Höhler, O. Pitois, F. Rouyer, A. Saint-Jalmes, and R. Flatman, *Foams: Structure and Dynamics*, edited by S. Cox (Oxford University Press, 2013), https://www.oxfordscholarship.com/view/10.1093/acprof:oso/9780199662890.001.0001/acprof- 9780199662890.

[16] E. Rio and A.-L. Biance, *Thermodynamic and Mechanical Timescales Involved in Foam Film Rupture and Liquid Foam Coalescence*, Chem. Phys. Chem. **15**, 3692 (2014).

[17] V. Miralles, B. Selva, I. Cantat, and M.-C. Jullien, *Foam Drainage Control Using Thermocapillary Stress in a Two-Dimensional Microchamber*, Phys. Rev. Lett. **112**, 238302 (2014).

[18] B. Selva, J. Marchalot, and M.-C. Jullien, *An Optimized Resistor Pattern for Temperature Gradient Control in Microfluidics*, J. Micromech, Microeng, **19**, 065002 (2009).

[19] D. Dedovets, C. Monteux, and S. Deville, *Five-Dimensional Imaging of Freezing Emulsions with Solute Effects*, Science **360**, 303 (2018).

[20] O. Bonhomme, B. Blanc, L. Joly, C. Ybert, and A.-L. Biance, *Electrokinetic Transport in Liquid Foams*, Adv. Colloid Interface Sci. **247**, 477 (2017).

[21] M. E. D. Zaniquelli and F. Galembeck, *Modification of Foam Drainage by Electroosmotic Effect*, Langmuir **1**, 647 (1985).

[22] A. Sharovarnikov, *Electrokinetic Properties of Foams*, Colloid J. USSR **46**, 77 (1984).

[23] B. Blanc, O. Bonhomme, P.-F. Brevet, E. Benichou, C. Ybert, and A.-L. Biance, *Electroosmosis Near Surfactant Laden Liquid–Air Interfaces*, Soft Matter **14**, 2604 (2018).

[24] A. H. Sheik, A. Trybala, V. Starov, and H. C. H. Bandulasena, *Electroosmotic Flow in Free Liquid Films: Understanding Flow in Foam Plateau Borders*, Colloid Interface **2**, 8 (2018).

[25] A. H. Sheik, H. C. H. Bandulasena, V. Starov, and A. Trybala, *Electroosmotic Flow Measurements in a Freely Suspended Liquid Film: Experiments and Numerical Simulations*, Electrophoresis **38**, 2554 (2017).

[26] S. Sett, R. P. Sahu, S. Sinha-Ray, and A. L. Yarin, *Experimental Investigation of Eletrokinetic Stabilization of Gravitational Drainage of Ionic Surfactants Films*, Electrochim. Acta **187**, 693 (2016).

[27] A. Sharovarnikov and V. Tsap, *Electroosmotic Transport of Liquid in Foams*, Colloid J, USSR **44**, 670 (1982).

[28] O. Bonhomme, O. Liot, A.-L. Biance, and L. Bocquet, *Soft Nanofluidic Transport in a Soap Film*, Phys. Rev. Lett. **110**, 054502 (2013).

[29] J. Israelachvili, *Intermolecular and Surface Forces*, 3rd ed. (Academic Press, New York, 2010).

[30] L. Joly, F. Detcheverry, and A.-L. Biance, *Anomalous ζ Potential in Foam Films*, Phys. Rev. Lett. **113**, 088301 (2014).

[31] V. Carrier, S. Destouesse, and A. Colin, *Foam Drainage: A Film Contribution?*, Phys. Rev. E **65**, 061404 (2002).

[32] N. Louvet, *Transport of Solid Particle in Liquid Foams: A Multiscale Approach*, Ph.D. thesis, Université Paris Est, 2009, 2009PEST1062.

[33] A.-L. Biance and O. Bonhomme, *Liquid Fraction Profile in a Liquid Foam under an Applied Voltage*, Phys. Rev. Fluids **3**, 110505 (2018).

[34] E. Brunet and A. Ajdari, *Generalized Onsager Relations for Electrokinetic Effects in Anisotropic and Heterogeneous Geometries*, Phys. Rev. E **69**, 016306 (2004).
[35] L. Onsager, *Reciprocal Relations in Irreversible Processes. I.*, Phys. Rev. **37**, 405 (1931).
[36] S. R. De Groot and P. Mazur, *Non-Equilibrium Thermodynamics* (Dover Publication Inc., New York, 2013).
[37] S. Berg, E. A. Adelizzi, and S. M. Troian, *Experimental Study of Entrainment and Drainage Flows in Microscale Soap Films*, Langmuir **21**, 3867 (2005).
[38] L. Saulnier, L. Champougny, G. Bastien, F. Restagno, D. Langevin, and E. Rio, *A Study of Generation and Rupture of Soap Films*, Soft Matter **10**, 2899 (2014).
[39] D. Weaire, S. Hutzler, G. Verbist, and E. Peters, *A Review of Foam Drainage*, Adv. Chem. Phys. **102**, 315 (1997).
[40] S. Cohen-Addad, R. Höhler, and O. Pitois, *Flow in Foams and Flowing Foams*, Annu. Rev. Fluid Mech. **45**, 241 (2013).
[41] G. Verbist, D. Weaire, and A. Kraynik, *The Foam Drainage Equation*, J. Phys. Condens. Matter **8**, 3715 (1996).
[42] E. M. Johnson and W. M. Deen, *Hydraulic Permeability of Agarose Gels*, AIChE J. **42**, 1220 (1996).
[43] V. Miralles, E. Rio, I. Cantat, and M.-C. Jullien, *Investigating the Role of a Poorly Soluble Surfactant in a Thermally Driven 2D Microfoam*, Soft Matter **12**, 7056 (2016).
[44] E. Forel, B. Dollet, D. Langevin, and E. Rio, *Coalescence in Two-Dimensional Foams: A Purely Statistical Process Dependent on Film Area*, Phys. Rev. Lett. **122**, 088002 (2019).
[45] D. M. Huang, C. Cottin-Bizonne, C. Ybert, and L. Bocquet, *Aqueous Electrolytes Near Hydrophobic Surfaces: Dynamic Effects of Ion Specificity and Hydrodynamic Slip*, Langmuir **24**, 1442 (2008).
[46] K. Tajima, M. Muramatsu, and T. Sasaki, *Radiotracer Studies on Adsorption of Surface Active Substance at Aqueous Surface. I. Accurate Measurement of Adsorption of Tritiated Sodium Dodecylsulfate*, Bull. Chem. Soc. Jpn. **43**, 1991 (1970).
[47] K. Feitosa, S. Marze, A. Saint-Jalmes, and D. J. Durian, *Electrical Conductivity of Dispersions: From Dry Foams to Dilute Suspensions*, J. Phys. Condens. Matter **17**, 6301 (2005).
[48] B. Derjaguin, N. Churaev, and V. Muller, *Surface Forces in Transport Phenomena*, in *Surface Forces* (Springer, New York, 1987), pp. 369–431.
[49] L. Fu, L. Joly, and S. Merabia, *Giant Thermoelectric Response of Nanofluidic Systems Driven by Water Excess Enthalpy*, Phys. Rev. Lett. **123**, 138001 (2019).
[50] V. Carrier and A. Colin, *Coalescence in Draining Foams*, Langmuir **19**, 4535 (2003).